Journal of Materials Chemistry C

Accepted Manuscript

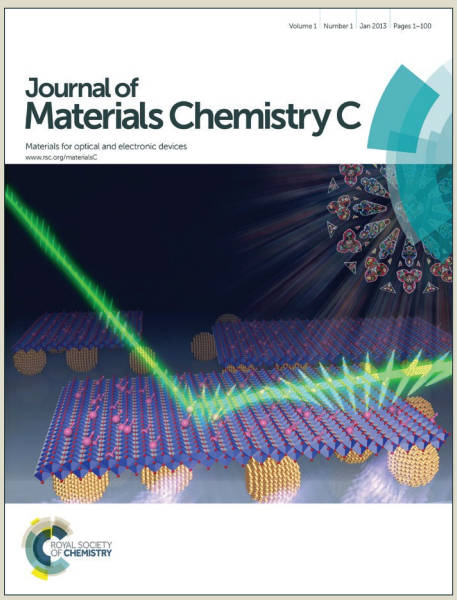

ROYAL SOCIETY OF CHEMISTRY

www.rsc.org/materialsC

Journal Name

RSCPublishing

ARTICLE

Control of electron transfer between Ce^{3+} and Cr^{3+} in $Y_3Al_{5-x}Ga_xO_{12}$ host by conduction band engineering

Cite this: DOI: 10.1039/x0xx00000x

Jumpei Ueda* [a,b,c], Pieter Dorenbos[c], Adrie J.J. Bos[c], Keisuke Kuroishi[a], Setsuhisa Tanabe[a]

Received 00th January 2012,
Accepted 00th January 2012

DOI: 10.1039/x0xx00000x

www.rsc.org/

Among inorganic compounds doped with lanthanide or transition metal ions for persistent phosphors, the transfer process of the localized electron in the dopant cations to the conduction band (CB) is crucial. In the $Y_3Al_{5-x}Ga_xO_{12}:Ce^{3+}$-$Cr^{3+}$, we found that the electron produced by photoionization of the Ce^{3+} ion by UV and blue excitation transfers to the Cr^{3+} ion through the CB. The electron trapped by Cr^{3+} is thermally released at different temperatures from 400 K to 150 K in the YAGG host with different Ga content because we managed to decrease the energy gap between the CB and the electron trap by increasing the Ga content. The persistent luminescence mechanism has been explained by constructing the vacuum referred binding energy (VRBE) diagram comprising the Ce^{3+}, Cr^{2+}, valence band (VB) and conduction band (CB) level energies in the YAGG host with different Ga/Al ratios.

1. Introduction

Control of the electron transfer from the dopant cation to the conduction band (CB) in inorganic compounds is important for all luminescent materials because such transfer causes quenching of the luminescence [1-5]. It is even more important for the persistent phosphors, which shows continuous luminescence from several minutes to hours after optical excitation has ceased. For charging and detrapping in such a phosphor, the electron is transferred between luminescent centers and traps via the CB[6-9]. By better understanding and control of the electron transfer, the design of high quantum efficiency phosphors and bright and long persistent phosphors becomes more effective.

Persistent phosphors have attracted a great deal of attention in luminous paints under indoor and outdoor environments and as biomarkers for in vivo imaging. The excitation light energy is stored temporally by trapping of charge carriers in the inorganic compounds and the energy comes out again as luminescence by recombination. For the application of persistent phosphors as luminous paint, blue and green light charging is preferred because lighting systems consisting of blue LEDs and visible phosphors does not include UV and violet light, and the solar spectrum has a peak at approximately 500 nm and does not have intense UV light compared with visible light. The most used persistent phosphor is $SrAl_2O_4:Eu^{2+}$–Dy^{3+} discovered by Matsuzawa et al. in early 1990's [10, 11]. After this discovery, many researchers tried to develop new persistent phosphors by co-doping Eu^{2+}-doped compounds with Ln^{3+} (Ln^{3+}: Dy^{3+}, Nd^{3+}) [11-15]. However, almost all persistent phosphors show the best persistent luminescence performance by UV light charging[16, 17]. To meet the recent demand in application of persistent phosphors, it is necessary to control various factors such as the charging excitation wavelength, the charging efficiency and the detrapping temperature. A material design guide for persistent phosphors does not yet exist. Recently, Dorenbos reported a method to construct an energy diagram containing conduction, valence bands, Ln^{2+} and Ln^{3+} in inorganic compounds, which is very helpful for understanding the persistent luminescence mechanism in Ln-doped compounds[6, 18]. Such method for compounds doped with transition metal ions is not available yet. There are also no reports about the optimum energy location of the excited state of a luminescence center with respect to the CB for an efficient charging process of persistent phosphors at room temperature. There are a few reports on the strategy to control the electron transfer efficiency and the detrapping temperature[5, 19-21].

In 2014, some of us successfully developed new persistent ceramic phosphors of $Y_3Al_2Ga_3O_{12}$(YAGG): Ce^{3+}-Cr^{3+}, with Ce^{3+}:5*d*-4*f* green luminescence (λ_{em}=505 nm) persisting for several hours after blue-light excitation[22]. In this persistent phosphor, the Ce^{3+} ions act as luminescence center and electron donor and the Cr^{3+} ions act as electron trap (electron accepter). This phosphor as a translucent ceramic sample shows quite intense persistent luminescence (208 mcd/m^2 20 min after 460nm excitation), which is comparable to that from a powder tablet of $SrAl_2O_4$: Eu^{2+}–Dy^{3+} phosphor.

In this study, we prepared $Y_3Al_{5-x}Ga_xO_{12}:Ce^{3+}$-$Cr^{3+}$ with wide range of Ga content (x=0~5) and investigated the charging and detrapping properties. It is expected that the energy location of the $5d_1$ level of Ce^{3+}, the electron trap by Cr^{3+} and the CB dramatically changes due to the changing band gap (7.7eV for $Y_3Al_5O_{12}$, 6.6 eV for $Y_3Ga_5O_{12}$). We found that the electron transfer efficiency as well as the ionization efficiency by blue excitation can be controlled by the Ga/Al ratio. We determined 0.2~0.3 eV as the optimum activation energy for electron release from the excited state of the luminescence center to CB. We also found that depending on the Ga/Al ratio the detrapping temperature varied in a wide range from 150 K to 400K, which correspond to a trap depth from 0.4 eV to 1.1 eV. From the constructed vacuum referred binding energy (VRBE) diagram

involving Ce^{3+}, Cr^{2+}, valence band (VB) and conduction band (CB) in the YAGG host with different Ga/Al ratio, it is found that the charging efficiency as well as the electron trap depth changes because the CB energy lowers. These results mean that we can design persistent phosphors by controlling the CB band energy. In addition, this material shows an electron trap depth distribution. The width of the trap depth distribution for a given Ga/Al ratio appears to depend on that ratio. It is explained by the cation-site environments around Cr^{3+} at the octahedral site of the garnet structure.

2. Experimental

Polycrystalline ceramics of $Y_3Al_{5-x}Ga_xO_{12}:Ce^{3+}$(0.5% at the dodecahedral {A} site)-Cr^{3+}(0.05% at the octahedral [B] site) and $Y_3Al_{5-x}Ga_xO_{12}:Ce^{3+}$(0.5% at the {A} site) with x=0, 1, 2, 2.5, 3, 3.5, 4, 5 and $Y_3Al_2Ga_3O_{12}:Cr^{3+}$(0.05% at the [B] site) were synthesized by solid-state reactions. The chemicals Y_2O_3 (99.99 %), Al_2O_3 (99.99 %), Ga_2O_3 (99.99 %), Cr_2O_3 (99.9 %) and CeO_2 (99.99 %) were used as starting materials. The powders were mixed by ball milling (Fritsch, Premium Line P-7) with ethanol. The obtained slurry was dried and pulverized, and then pressed at 50 MPa into 10-mm-ϕ X 2-mm thick pellets. The pellets were sintered at 1600 °C for 12 h in air. The crystal phase was identified as a single phase of the garnet structure using X-ray diffraction measurement system (Rigaku, Ultima IV). Thermoluminescence (TL) measurements above room temperature (298 - 823 K) were performed with a RISØ TL/OSL reader model DA-15 and a controller model DA-20. The luminescence observed during the TL experiments was detected with a 2 mm BG-39 filter (transmission between 320 nm and 650 nm) placed in front of an EMI9635QA photomultiplier tube (PMT). Samples were irradiated with a $^{90}Sr/^{90}Y$ beta source with a dose rate of 0.7 mGy/s. All measurements were executed under a flow of nitrogen gas. For the thermoluminescence excitation spectra, the samples were illuminated with monochromatic light obtained from a Xe lamp (Newport, 66921) and a monochromator (Newport, 74004), and after the illumination phase the TL glow curve was measured. The procedure was repeated by stepping the monochromator through a chosen wavelength range. For the measurement of a TL emission spectrum as a function of temperature, the samples were first irradiated with γ-rays from a ^{60}Co source with a dose rate of 1.4kGy/h, after that TL glow curve were measured via an Ocean Optics, QE65000 spectrometer. Low temperature thermoluminescence measurements (90 - 450 K) were recorded with a sample chamber operating under vacuum (P = 10^{-7} mbar), a $^{90}Sr/^{90}Y$ beta irradiation source with a dose rate of ~0.4m Gy/s and a PerkinElmer channel PM tube (MP-1393). Liquid nitrogen was used as cooling medium. A small piece of the pellet was attached to the copper heater element with a thin layer of silver paint (Busch 5900). The Ce^{3+} luminescence during TL readout was collected via a 2 mm BG-39 filter in the front of the PMT. Photoluminescence excitation (PLE) spectra in the VUV region were measured using a D_2 lamp (Hamamatsu photonics, L1835) and a monochromator (Acton research cooperation, VM 502) and a detection system using a monochromator (Princeton instruments, Acton SP 23000) and a PMT (Hamamatsu, H10330A-75). The temperature dependence of photoluminescence (PL) was measured with the RISØ TL/OSL reader model DA-15 and the QE65000 spectrometer above room temperature by 420 nm excitation, which is the same light source as in the TLE measurement. For the temperature dependence of PL below room temperature, samples were mounted on a cryostat (SHI-APD, DE-204SLFF). The samples were excited by monochromatic light that was obtained from a Xe lamp (Newport, 66921) and a monochromator (Horiba Jobin Yvon, GEMINI180). The luminescence was detected by the same system as used for the PLE spectra. All the spectra in this study were calibrated using a standard halogen lamp and a standard Si photodetector.

3. Results

3.1 Photoluminescence properties

Figure 1 shows the temperature dependence of the integrated intensity of the Ce^{3+}:$5d_1$-$4f$ PL band in the Ce^{3+}-singly-doped $Y_3Al_{5-x}Ga_xO_{12}$ (YAGG) samples with x=0, 1, 2, 2.5, 3, 3.5, 4. All the YAGG:Ce samples show temperature quenching curves according to the single barrier quenching function,

$$\frac{I(T)}{I_0} = \frac{1}{1+\Gamma_0/\Gamma_v exp(-E_q/kT)} \quad (1),$$

where, I is the luminescence intensity, Γ_v is radiative decay rate, Γ_0 is the attempt rate of the non-radiative process, E_q is the activation energy, k is the Boltzmann constant and T is the temperature. Based on the fitting by *E*q. (1), thermal quenching parameters were estimated as shown in Table 1. The activation energy (E_q) and Γ_0/Γ_v decreases with increasing Ga content. Quenching temperature ($T_{50\%}$), at which the luminescence intensity is 50% of the intensity at low temperatures, were also estimated from the temperature quenching curves. $T_{50\%}$ monotonically decreases from 640 K in the x=0 sample to 301 K in the x=4 sample with increasing Ga content. From our previous photoconductivity research, it is found that these quenching is caused by the thermal ionization process[1].

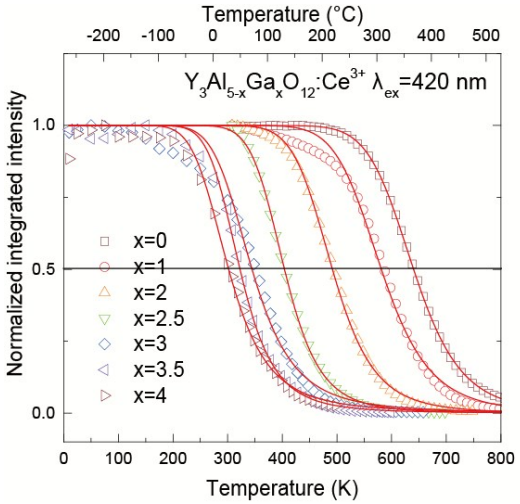

Fig. 1. Normalized ($I(T)/I_0$) PL intensity of Ce^{3+}-doped YAGG samples (x=0, 1, 2, 2.5, 3, 3.5, 4) by 420 nm excitation as a function of temperature.

Figure 2 shows the PLE spectra in the VUV region of Ce^{3+}:$5d_1$-$4f$ luminescence at 510 nm for the YAGG:Ce-Cr (x=0, 1, 2, 2.5, 3, 3.5, 4) samples. A PLE band is observed in the range between 200 nm and 250 nm in all the samples. This band is attributed to the transitions from the $4f$ ground state of Ce to its third ($5d_3$), fourth ($5d_4$) and fifth ($5d_5$) $5d$ levels. The PLE edges below 220 nm are attributed to the host exciton bands that energy transfers to a nearby Ce^{3+} ion [23, 24]. Beyond those edges at shorter

wavelength the excitation is saturated. The energy of the fundamental absorption edge lowers with increasing Ga content. Using a Tauc plot of the direct allowed transition, the fundamental absorption energies of the near Ce^{3+} host exciton bands, E_{ex_FACe}, in the YAGG hosts were estimated and shown in Table 1.

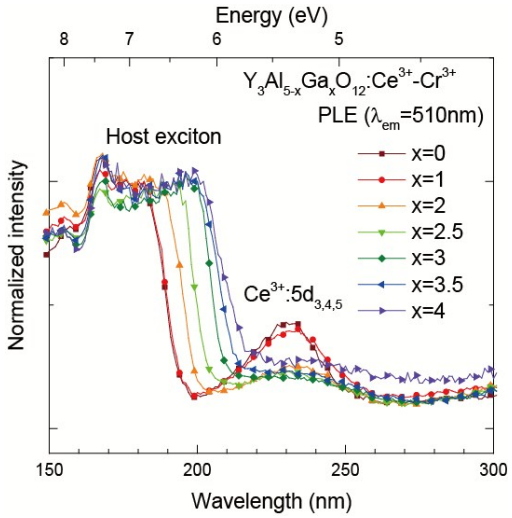

Fig. 2. PLE spectra monitoring luminescence at 510 nm of various YAGG:Ce-Cr samples in VUV region at room temperature.

Figure 3 shows the PLE spectra of Cr^{3+}:^{2}E-^{4}A$_2$ luminescence at 693 nm in the YAGG:Ce-Cr samples. A PLE band with a clear maximum is observed in the range between 180 nm and 220 nm in each sample. These PLE bands can be attributed to the host exciton that energy transfers to a nearby Cr^{3+}. The energy shifting of the peak energy of the host exciton band in the PLE of Cr^{3+} as a function of Ga content has same tendency to the host exciton in the PLE of Ce^{3+} as shown in Table 1. This consistency supports that the PLE bands between 180 nm and 220 nm in the PLE spectra of Cr^{3+} is due to near defect host exciton bands. The exciton energy related to Cr^{3+} luminescence is about 0.65 eV lower than that to Ce^{3+} luminescence reported in the paper by Zorenko et al [25] .

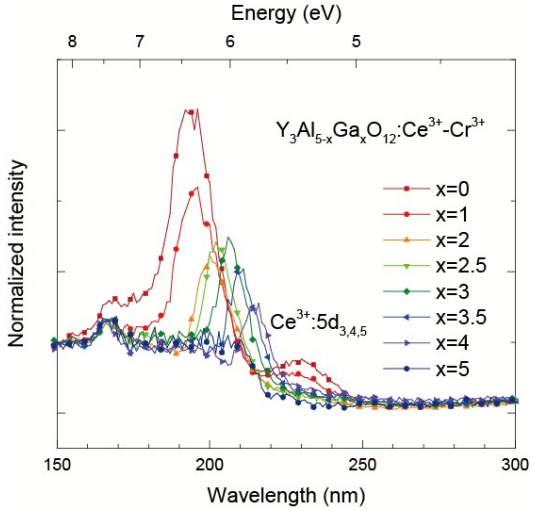

Fig. 3. PLE spectra monitoring luminescence at 693 nm of various YAGG:Ce-Cr samples in VUV region at room temperature.

Figure 4 shows the PLE spectrum of the Cr^{3+}-single-doped YAGG (YAGG:Cr) with x=3 monitoring Cr^{3+} luminescence at 693nm. The broad PLE bands at 630 nm, 450 nm and 280 nm are attributed to the d-d transitions of Cr^{3+} from $^4A_2$ to $^4T_2$, $^4T_1(^4F)$ and $^4T_1(^4P)$, respectively. The PLE band at around 220 nm is due to the near Cr^{3+} host exciton because of the coincidence with the host exciton band in the PLE of Cr^{3+} for the YAGG:Ce-Cr samples.

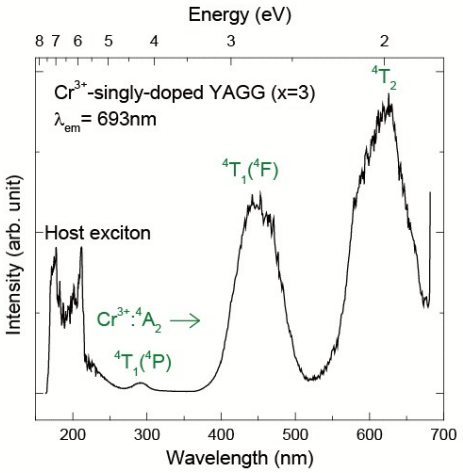

Fig. 4. PLE spectrum monitoring 693 nm of YAGG:Cr (x=3) in the range between 150 nm and 690 nm at room temperature.

Table 1. Quenching temperature, $T_{50\%}$, activation energy of quenching, E_q, ratio of attempt rate and radiative rate, Γ_0/Γ_v, from the luminescence quenching curve and fundamental absorption energy of host exciton that energy transfers to Ce^{3+}, E_{ex_CeFA} , and host exciton peak energy that energy transfers to Cr^{3+}, E_{ex_Cr}, from PLE analysis in the $Y_3Al_{5-x}Ga_xO_{12}$ host with different Ga content x.

x	$T_{50\%}$ (K)	E_q (eV)	Γ_0/Γ_v	E_{ex_CeFA} (eV)	E_{ex_Cr} (eV)
0	640	0.81	2.27 X 10^6	6.46	6.39
1	583	0.65	4.86 X 10^5	6.44	6.33
2	491	0.55	3.86 X 10^5	6.26	6.20
2.5	404	0.43	2.49 X 10^5	6.15	6.14
3	344	0.28	1.08 X 10^5	5.98	6.02
3.5	323	0.26	1.07 X 10^5	5.87	5.90
4	301	0.21	3.88 X 10^3	5.79	5.76

3.2 Thermoluminescence properties

Figure 5 shows the thermoluminescence intensity of YAG:Ce-Cr (x=0) after γ-irradiation as a function of emission wavelength and temperature. An intense TL glow is observed around the position (150°C, 550 nm). From the TL emission spectrum at 150°C as projected on the right side of Fig. 5 , the peak at 550 nm originates from the Ce^{3+}:$5d_1$-$4f$ emission. In this emission spectrum, the weak Cr^{3+}: ^{2}E-^{2}A$_2$ luminescence at around 700 nm is also observed. By comparison of the TL glow curves of Ce^{3+} and Cr^{3+} luminescence at different emission wavelength as projected above Fig. 5, the same TL glow peaks at approximately 150°C are observed in both cases. From this we conclude that the traps responsible for the TL of Ce^{3+} and Cr^{3+} emission are identical. This results supports that the Cr^{3+} thermoluminescence emission (persistent luminescence) is caused by energy transfer from Ce^{3+} to Cr^{3+}as mentioned in our previous work[26].

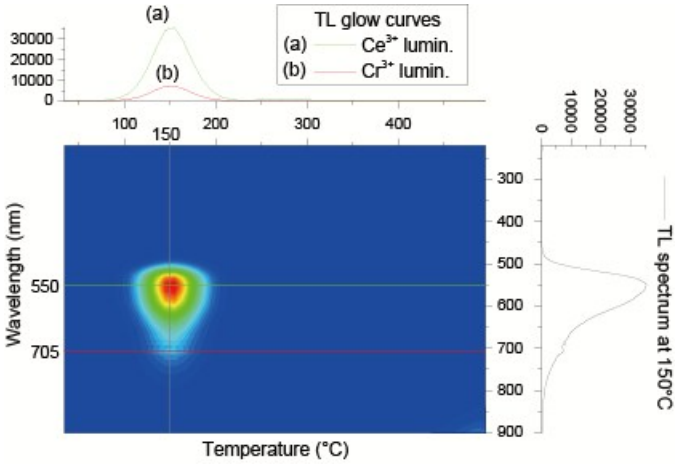

Fig. 5. Contour plot of the TL intensity of YAG:Ce-Cr (x=0) sample after γ-irradiation as a function of wavelength and temperature. The projection above shows the TL glow curves of Ce^{3+} luminescence (a) and Cr^{3+} luminescence (b) and the projection to the right shows TL emission spectrum at 150 °C. Glow curves were recorded at a heating rate of 5 K/s.

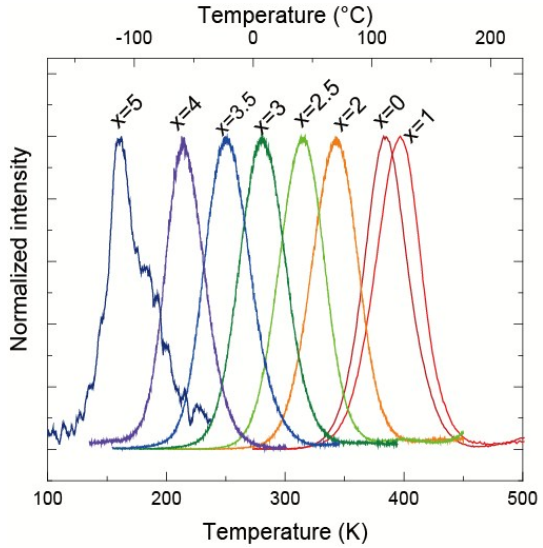

Fig. 6. Thermoluminescence glow curves at a heating rate of 10 K/min after β-irradiation of the YAGG:Ce-Cr samples with x=0, 1, 2, 2.5, 3, 3.5, 4 and 5 composition. The glow curves shown are corrected for thermal quenching using the curves shown in Fig. 1.

Normalized TL glow curves of the YAGG:Ce-Cr samples after β-irradiation are shown in Fig. 6. As discussed by many researchers, the shape and the maximum position of TL glow curves will be affected by the thermal quenching of recombination luminescence [27]. All the TL glow curves except the curve for the YGG:Ce-Cr (x=5) sample were corrected by dividing the TL intensity by the Ce^{3+} PL intensity at each temperature as reported in Fig. 1. The observed single TL peak can be attributed to the electron trap of Cr^{3+} ($Cr^{3+} + e^-$), which is regarded as the state of Cr^{2+} (we will discuss later in discussion section 4.1). The peak temperature of the TL glow curve except for the x=0 sample lowers with increasing Ga content as shown in Table 2. In order to estimate the trap depth, the variable heating rate plot method was applied as shown in Fig. 7. (N.B. the heating rate method is valid even in the case that the material has a trap depth distribution that will be discussed later. See supporting information.) The trap depths remain almost the same up to x=2 and then decreases with increasing Ga content as shown in Table 2. The frequency factor spreads between 10^{11} and 10^{13} s^{-1} which are typical for the lattice vibrational frequencies. The FWHM (full width at half maximum) of the TL glow curves in Fig. 6 firstly increases and later decreases with increasing Ga content. According to a first-order Randall–Wilkins glow curve [28-30] using the obtained parameters from the heating rate method, the FWHM of a TL glow curve should become narrower with decreasing electron trap depth (See supporting information). Moreover they are expected to be asymmetric while the glow curves in Fig 6 are relatively symmetric. We explain this behavior by assuming that the traps in YAGG:Ce-Cr do not have a single depth but shows a trap depth distribution with a width in energy that depends on Ga content x.

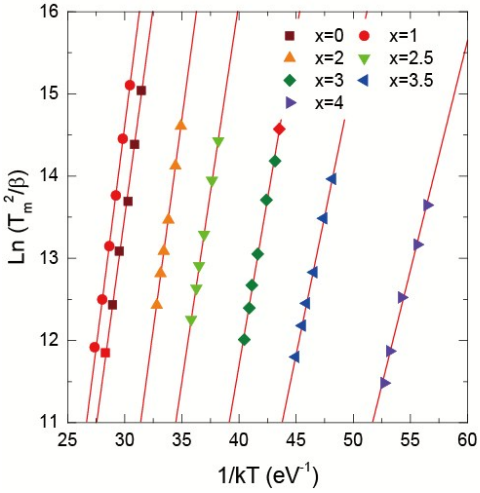

Fig. 7. Heating rate plot of the TL glow peak temperature T_m in YAGG:Ce-Cr samples

Table 2. Peak temperature, T_m, of the luminescence quenching corrected TL glow curves recorded with 10 K/min heating rate. The trap depth and the frequency factor estimated from the variable heating rate plot in $Y_3Al_{5-x}Ga_xO_{12}$:Ce-Cr with different Ga content x. *Trap depth for x=5 is estimated using 1st order kinetics.

x	T_m (K)	Trap depth (eV)	Frequency factor (s^{-1})
0	384	1.02	3.2×10^{11}
1	396	1.08	6.7×10^{11}
2	343	1.02	1.8×10^{13}
2.5	314	0.92	1.2×10^{13}
3	279	0.81	1.0×10^{13}
3.5	249	0.67	8.6×10^{11}
4	214	0.56	3.9×10^{11}
5	161	0.41*	-

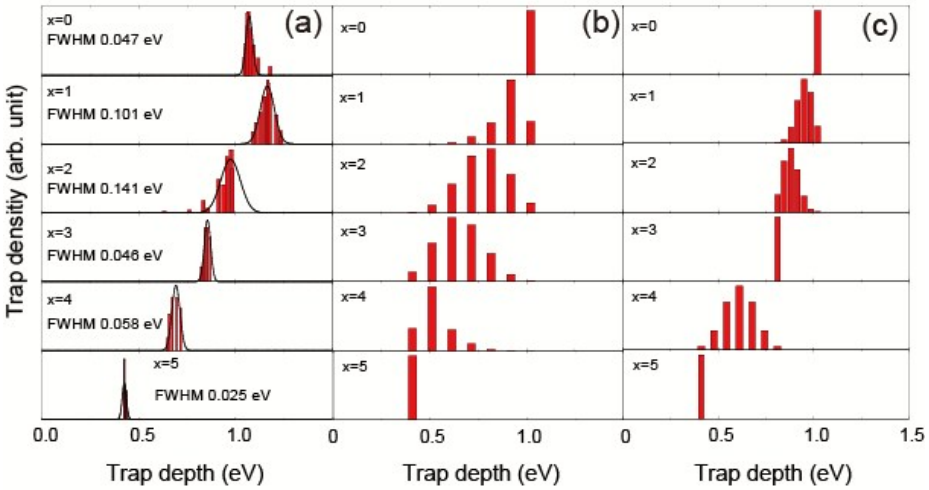

Fig. 8. Trap depth distribution in the YAGG:Ce-Cr samples (x=0, 1, 2.5, 3, 3.5, 4, 5) derived from (a) the measured TL glow curves, (b) derived from simulation by assuming a random occupation Ga on tetrahedral and octahedral sites and (c) derived from simulation by assuming that first the tetrahedral sites are randomly occupied by Ga and after full occupation the octahedral sites.

In order to determine the trap depth distribution, the pre-heating method for estimation of trap depth values and the initial rise method for estimation of trap depth as reported by Van den Eeckhout *et al.* [31] were applied for all the samples except YGG:Ce-Cr as shown in Fig. 8 (a). (See supporting information for details.) Only for the YGG:Ce-Cr (x=5), the signal over noise (S/N) ratio of the initial part of the TL glow curve is poor as shown in Fig. 6 because of a very low quantum efficiency of PL in YGG:Ce. Because the TL glow peak temperature can still be obtained with good accuracy, for this sample the trap depth was estimated assuming 1st order kinetics and using Eq.(2) below.

$$\frac{\beta E}{kT_m{}^2} = s\exp(-\frac{E}{kT_m}) \qquad (2).$$

If the frequency factor, s, is known, the trap depth, E, can be determined using numerical computation methods.

For the YGG:Ce-Cr(x=5) sample, the same frequency factor of 3×10^{13} as for YAGG:Ce-Cr(x=4) sample was used. The then estimated trap depth from the TL glow curves with 10 K/s heating rate as shown in Fig. 6 becomes 0.41 eV. The trap depth distribution of the x=5 sample is also shown in Fig. 8 (a). For each sample, except for x = 2, it has a Gaussian shape. With increasing Ga content, the center of the trap distribution shifts, except for the YAGG:Ce-Cr(x=1) sample, to lower energy. The width of the trap distribution becomes maximum for x=2, and then decreases again.

The trap depth distribution is assumed to be caused by variations in the environment of the defect responsible for the trap. In YAGG:Ce-Cr, Cr^{3+} ions at octahedral sites can act as electron traps. The anion and anion vacancy distribution around the Cr ions will be regarded the same in all the different samples. We will only consider the distribution of cations at the nearest cation sites around the octahedral Cr-site. Fig. 9(a) shows the first and second nearest cation sites around an octahedral Cr-site. The octahedral site shares corners with six tetrahedral sites and edges with six dodecahedral sites. The dodecahedral sites are always occupied by Y ions in the YAGG:Ce^{3+}-Cr^{3+} samples and occasionally by a Ce ion. The tetrahedral sites are occupied by Al and Ga. Fig. 9 (b) illustrates possible occupancy combination (c_i) by Ga ions in the six tetrahedral sites around a Cr^{3+} octahedral site and i is the number of sites occupied by Ga. Here, we focus only on the number of Ga ions in the nearest tetrahedral sites and we do not take into account the actual position of the Ga ions. For the $Y_3Al_5O_{12}$:Ce-Cr and $Y_3Ga_5O_{12}$:Ce-Cr samples, all the tetrahedral sites are occupied by either zero or six Ga ions. There is no cation disorder in the tetrahedral sites and consequently the trap depth distribution is minimal. However, in all the other YAGG:Ce^{3+}-Cr^{3+} samples, all seven Ga occupancy combinations as shown in Fig. 9 (b) can co-exist. The probability P_i of each combination c_i is given by the binomial distribution function Eq. (3).

$$P_i = \binom{6}{i}\left(\frac{5-x}{5}\right)^{6-i} \times \left(\frac{x}{5}\right)^{i} \qquad (3)$$

Here, we assumed that Ga ions occupy both octahedral and tetrahedral sites with the same probability x/5. Each combination is related with a specific trap depth. The combinations c_0 and c_6 correspond to the trap depth of YAG:Ce-Cr (1.02 eV) and YGG:Ce-Cr (0.41 eV) estimated in Table 2,. We will estimate the trap depths of the other combinations from the interpolation between c_0 and c_6. From P_i and the corresponding trap depth for each c_i, the trap depth distributions as shown in Fig. 8 (b) are obtained. In this result, the width of the trap depth distribution firstly increases, and then decreases with increasing Ga content. However, this tendency is different from the experimental result in Fig. 8 (a).

From the results of X-ray diffraction refinement by Marezio et al. and Nakatsuka et al., Ga^{3+} preferentially occupies the tetrahedral site rather than the octahedral site in the YAG-YGG solid solution [32, 33]. If the Ga ions first start to occupy the tetrahedral sites, the trap depth distribution will start to increase initially and become small again at x=3 because then all tetrahedral sites will be occupied by Ga. The experimental results support the selective occupation of the tetrahedral sites because the width of the trap distribution indeed narrows again at x=3. If only the nearest tetrahedral sites would affect the trap depth distribution then for x=3, 4 and 5 the distribution will remain constant. This is not observed, which suggests that the nearest octahedral sites also need to be taken into account for the trap depth distribution. Fig. 9 (c) illustrates the six nearest tetrahedral sites plus the in total six nearest octahedral sites around an octahedral Cr^{3+} site. Fig. 8 (c) shows the simulated trap depth distributions in the situation where Ga ions first start to occupy randomly the tetrahedral site and after completely filling of those the octahedral ones. For this simulation, we used

the probabilities P_i estimated by the same method as shown in Table 3 and interpolated trap depth using YAG:Ce-Cr (1.02 eV), $Y_3Al_2Ga_3O_{12}$:Ce-Cr(0.81 eV) and YGG:Ce-Cr (0.41 eV). The now obtained trap distributions are in good agreement with the experimental results in Fig. 9(a).

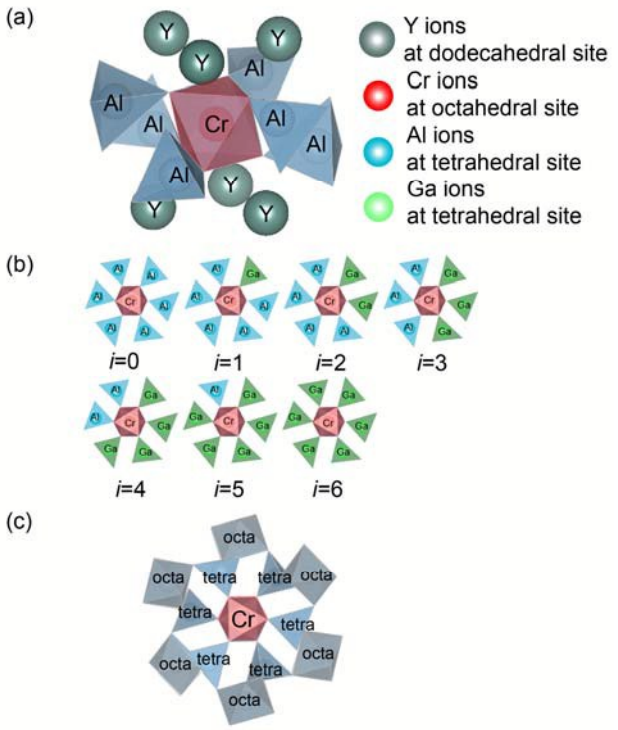

Fig. 9. (a) The cation coordinations around an octahedral Cr^{3+}-site, (b) combinations of first-nearest tetrahedral site occupation by Ga, c_i (i is equal to the number of Ga ions in the nearest tetrahedral sites), and (c) illustration of the first six nearest tetrahedral sites and six octahedral sites around an octahedral Cr-site.

Table 3. Probability P_i (in %) of different cation distribution combinations c_i (i= 1, …,6 as shown in Fig. 9) in $Y_3Al_{5-x}Ga_xO_{12}$ with different Ga content x.

i	x=0	x=1	x=2	x=3	x=4	x=5
0	100	26.21	4.67	0.41	0.01	0
1	0	75.37	18.66	3.69	0.15	0
2	0	24.58	31.10	13.82	1.54	0
3	0	8.19	27.65	27.65	8.19	0
4	0	1.54	13.82	31.10	24.58	0
5	0	0.15	3.69	18.66	75.37	0
6	0	0.01	0.41	4.67	26.21	100

3.3 Charging efficiency

Figure 10 shows thermo-luminescence excitation (TLE) or the charging spectra by monitoring the Ce^{3+} recombination luminescence in the YAGG:Ce-Cr(x=0, 1, 2, 2.5, 3) samples. In all the samples, TLE bands were observed at around 340, 270 and 230 nm. The band at 340 nm is attributed to the $4f$-$5d_2$ Ce^{3+} excitation. Only in the x=2.5 and 3 samples, the intense TLE band attributed to the $4f$-$5d_1$ transition of Ce^{3+} appears at around 420 nm. These results show that samples with x ≥ 2.5 can store electrons efficiently by blue light illumination at room temperature.

Assuming that thermal quenching proceeds by thermal ionization, the thermal ionization efficiency, η_{ti}, can be defined as ($1-I_{(300K)}/I_0$) or using Eq. (4)

$$\eta_{ti} = \frac{\frac{\Gamma_0}{\Gamma_v}\exp(-\frac{E_q}{kT})}{1+\frac{\Gamma_0}{\Gamma_v}\exp(-\frac{E_q}{kT})} \text{ at T} = 300 \text{ K} \qquad (4).$$

The upper panel of Fig. 11 shows η_{ti} at 300 K after excitation to the $5d_1$ level as calculated from the quenching curves. The lower panel shows the integrated intensity of the $5d_1$ and $5d_2$ TLE bands in Fig. 10 as a function of Ga content x. With increasing Ga content, both the thermal ionization efficiency and the integrated intensity of the $5d_1$ TLE bands of Ce^{3+} increases rapidly above x=2.5. This result evidences that the thermal ionization from Ce^{3+} $5d_1$ level causes the charging in the persistent luminescence mechanism. The integrated intensity of the $5d_2$ TLE band starts to increase above x=1 Ga content. This is because the $5d_2$ level is located above the $5d_1$ level and consequently has smaller activation energy for thermal ionization.

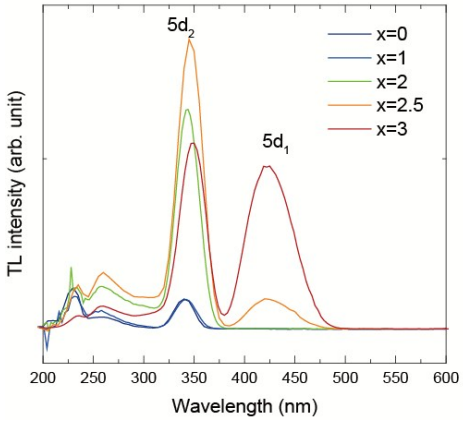

Fig. 10. Thermo-luminescence excitation spectra of the Ce-Cr-doped YAGG samples.

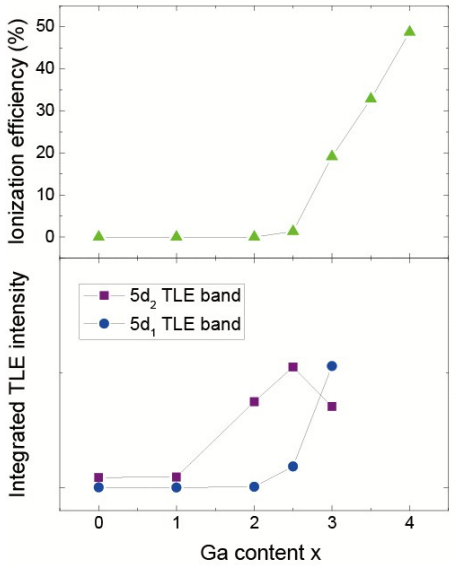

Fig. 11. Ionization efficiency from the $5d_1$ level (upper panel) and TLE intensity of the $5d_1$ and $5d_2$ bands (lower panel) as a function of the Ga content.

Figure 12 shows TL glow curves of YAGG:Ce-Cr (x=0, 2) recorded after 350 nm ($5d_2$) or 420 nm ($5d_1$) illumination at various pre-heating temperatures. In these measurements, the sample was first illuminated by 350 nm or 420 nm photons at the pre-heating temperature Next, after cooling down to room temperature, the TL glow curves were measured. In the TL glow curve of the x=0 sample after 350 nm illumination, the TL intensity increases with increasing pre-heating temperature. This means that the charging process is caused by a thermally activated ionization process. In the TL glow curve of the x=2 sample after 350 nm illumination, the TL intensity keeps constant and then decreases with increasing pre-heating temperature. For x=2, there is no thermal ionization process anymore. The charging process for the x=2 sample during 420 nm illumination is again caused by a thermal ionization because the TL intensity increases with increasing temperature. From these results, it is found that the Ce^{3+}:$5d_2$ level in YAG and Ce^{3+}:$5d_1$ level in YAGG (x=2) is located below the bottom of the CB while Ce^{3+}:$5d_2$ in YAGG (x=2) is located above the bottom of the CB.

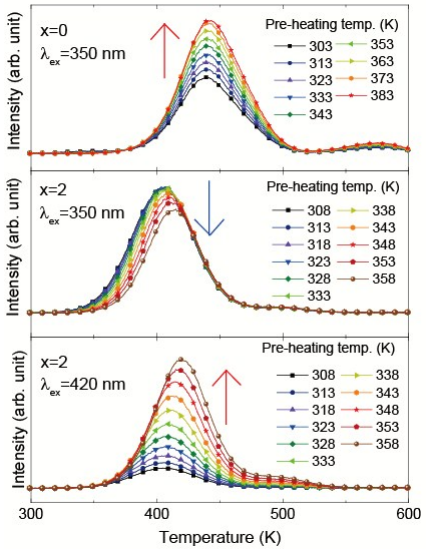

Fig. 12. TL glow curves of the YAGG:Ce-Cr (x=0) sample after 350 nm illumination and the YAGG:Ce-Cr (x=2) sample after 350 nm or 420 nm illumination. Illumination occurred at the indicated pre-heating temperature.

4. Discussion

4.1 Vacuum referred binding energy (VRBE) diagram

For the discussion of the charging and the detrapping processes, it is helpful to know the vacuum referred binding energy (VRBE) diagram of Ce^{3+} - Cr^{3+} codoped $Y_3Al_{5-x}Ga_xO_{12}$. Dorenbos reported how to construct the VRBE diagram of compounds and presented the VRBE diagram of the $Y_3Al_{5-x}Ga_xO_{12}$ garnets doped with Ce^{3+} [18, 34]. There is no data for the $Y_3Al_{5-x}Ga_xO_{12}$:Ce^{3+} with x=2.5 and 3.5 and no information on the VRBE of the trapped electron in the Cr ion.

We estimated the mobility band gap energy 8% bigger than the host exciton creation energy according to the paper by Dorenbos [35]. In the garnet crystals, the host exciton creation energy E^{ex} can be estimated from the PLE spectrum of different types of excitonic emission or lanthanide emission at low temperature. E^{ex} for YAG and YGG are known from the spectroscopy of excitonic emission [25, 35-37]. For YAGG with different Ga content, Mayolet *et al.* reported the host exciton energy based on the PLE spectra of Tb luminescence [38]. To determine the host exciton creation energy and the systematic variation therein for YAGG with different Ga content, we prefer to estimate the values from PLE spectra monitoring the same luminescence using the same measurement system. In this work, E^{ex} was estimated from the PLE spectra of Ce^{3+} in the VUV region as shown in Fig. 2. It shows a clear systematic energy shift of the fundamental absorption edge attributed to the near Ce-defect host exciton creation as a function of Ga content. Between the fundamental absorption onset of the host excitation and the peak maximum of the host exciton peak in $Y_3Al_5O_{12}$, there is 0.49 eV difference at 15 K in our result (not shown here). There is also 0.15 eV difference between the energies of the fundamental absorption edges at 15 K and 300 K. Therefore, a value of 0.64 eV will be added to the observed fundamental absorption edge energy at 300K to estimate E^{ex} at low temperatures. Results are shown in column 2 of Table 4. 6.77 eV as reported by Dorenbos for $Y_3Al_{5-x}Ga_xO_{12}$ was used for the energy separation U(6,A) between the Eu^{2+} and Eu^{3+} ground states in the VRBE scheme [34]. The energy of charge transfer E^{CT} from the valence band to Eu^{3+} are as in [9] obtained from Jia *et al.* [39] For x=1, x=2.5 and x=3.5, E^{CT} was estimated by interpolation from data for x=0, 2, 3 and 4. For the *4f-5d* transition energies of Ce^{3+}, we used the values from our previous work [40]. The VRBE of an electron in the Cr^{2+} ground state, E_{Cr2+}, which could be electron trap level, can also be estimated from the energy of charge transfer (CT) from the valence band to Cr^{3+}. Different CT energies in YAG:Cr^{3+} at 230 nm (5.39 eV) [41] and at 180~250 nm (6.89 eV~4.96 eV) [42] have been reported by Wang *et al.* and Yamaga *et al.*, respectively. These results show that the Cr^{2+} energy level is located just below the bottom of CB and acts as an electron trap level. In our sample, YAGG:Cr (x=3), the peak of the CT band was not observed clearly because the CT band and host related exciton bands overlap. Therefore, in this study, we simply subtracted the trap depth energy in column 3 of Table 2 from the energy E_C at the bottom of the conduction and in column 4 of Table 4 to estimate E_{Cr2+} as compiled in column 7 of Table 4. All required input parameters to create the VRBE diagrams are compiled in Table 4. The stacked VRBE diagram of the YAGG:Ce-Cr with various Ga content (x=0, 1, 2, 2.5, 3, 3.5, 4 , 5) is shown in Fig. 13.

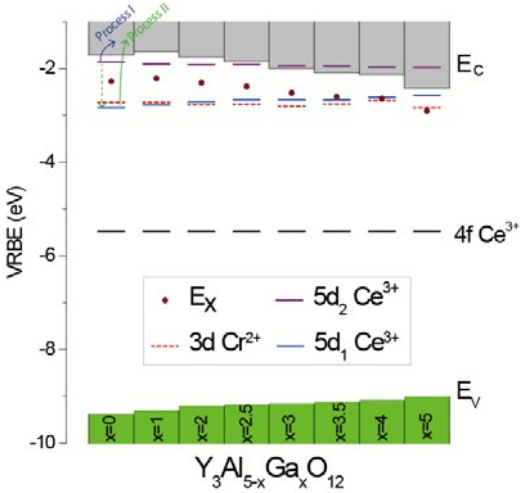

Fig. 13. Stacked VRBE diagram of $Y_3Al_{5-x}Ga_xO_{12}$:Ce-Cr (x=0, 1, 2, 2.5, 3, 3.5, 4, 5).

Table 4. Host exciton creation energy, E_{ex}, at low temperature and charge transfer energy of Eu^{3+}, E^{CT}, energy gap between Ce^{3+}:$5d_1$ and CB, $E_{5d1\text{-}CB}$, and VRBE of valence band, E_v, and conduction band, E_c, Ce^{3+}:$5d_1$ and $5d_2$, E_{Ce5d1} and E_{Ce5d2}, and Cr^{2+}, E_{Cr2+} in the $Y_3Al_{5-x}Ga_xO_{12}$ host (in eV).

x	E^{ex}	E^{CT} [a]	E_v	E_c	E_{ce5d1}	E_{Ce5d2}	E_{Cr2+}	$E_{5d1\text{-}CB}$
0	7.10	5.42	-9.37	-1.70	-2.84	-1.86	-2.73	1.13
1	7.08	5.34	-9.16	-1.64	-2.78	-1.90	-2.59	1.14
2	6.90	5.25	-9.20	-1.75	-2.71	-1.93	-2.77	0.96
2.5	6.79	5.22	-9.17	-1.84	-2.66	-1.92	-2.76	0.82
3	6.62	5.19	-9.14	-1.99	-2.66	-1.94	-2.80	0.67
3.5	6.51	5.16	-9.11	-2.08	-2.67	-1.95	-2.75	0.58
4	6.43	5.12	-9.07	-2.13	-2.62	-1.98	-2.69	0.49
5	6.10 [b,c]	5.05	-9.00	-2.41	-2.57	-1.98	-2.84	0.16

a Jia et al. (2005)[39]
b Zorenko et al. (2009)[37]
c Dorenbos (2013)[35]

E_{Cr2+} in YAGG except YGG appears always near -2.75 eV ± 0.06eV, see column 7 in Table 4. Dorenbos and Rogers reported that the VRBE of the single electron in the lowest energy 3d, 4d, and 5*d* levels in group IIIa, IVa, Va and VIa transition metal (TM) and lanthanide (Ln) ions in different compounds tends to spread ±1 eV around a mean value typical for that TM or Ln element [43-46]. The VRBE of the single electron in the lowest 5*d* level of Ce^{3+}, E_{Ce5d1}, are located between -2.57 and -2.84 in the YAGG host, see column 5 in Table 4. The spread of ±0.14 eV is smaller than the ±1 eV because all the YAGG compounds are very similar. Cr^{2+} has $3d^4$ electron configuration, and within the very related garnet family of YAGG it now appears that E_{Cr2+} is rather constant despite much larger changes in E_V and E_C.
One may compare E_{Cr2+} in our garnets with that in Al_2O_3 as estimated from the 6.92 eV VB to Cr^{3+} CT energy reported in [47-49]. With E_V = -9.8 eV in Al_2O_3 [34] E_{Cr2+} is estimated at -2.88 eV which is quite similar to that in our YAGG system, see column 7 in Table 4. This suggests that the VRBE of an electron in the Cr^{2+} $3d^4$ ground state on an octahedral site is fairly independent on type of compounds, and it also confirms that Cr^{2+} is the electron trap level in this material.

4.1 Charging and detrapping processes

The stacked VRBE diagram of Fig. 13 reveals that the energy gap between the $5d_1$ level and the CB decreases with increasing Ga content. This is consistent with the thermal quenching data of Fig. 1, which supports that the quenching is caused by the thermal ionization process in YAGG:Ce^{3+}. Compared with E_q in column 3 of Table 1, $E_{5d1\text{-}CB}$ in column 8 of Table 4 is always 0.35 ± 0.05 eV larger. Such systematic errors are well possible because the VRBE is constructed based on the state before lattice relaxation while the estimated activation energy is based on the state after lattice relaxation. In Fig. 11, we showed that the charging probability from the $5d_1$ level to the trap is correlated with the thermal ionization efficiency given by Eq. (4). E_q and also $E_{5d1\text{-}CB}$ are regarded as important energies that determine the charging probability. The trap depth determines the de-trapping efficiency. The TL excitation spectra and glow curves of YAGG:Ce-Cr(x=2) in Fig. 10 and Fig. 12, demonstrated that this sample can be charged by blue light illumination although the charging efficiency is poor. The thermal ionization efficiency of this sample was estimated 0.03% from Eq. (4) with an activation energy E_q of 0.55 eV (see Table 1). Below 0.03% ionization efficiency, thermoluminescence cannot be observed in our equipment. Apparently 0.55 eV is the activation energy at which ionization efficiency at room temperature becomes too poor to have significant charging of the traps and thermoluminescence is not detected in our measurement. In the VRBE diagram, this threshold energy for the charging is 0.9 ± 0.05 eV because $E_{5d1\text{-}CB}$ was found 0.35 eV larger than E_q

Figure 11 shows that the ionization efficiency exceeds 20% for x=3 corresponding with E_q=0.28 eV and $T_{50\%}$=344K. For higher Ga content ionization efficiency increases but at the same time the luminescence efficiency decreases and for x>4 the quenching temperature $T_{50\%}$ shifts to below RT. Clearly there must be an optimum value for E_q, a value that is small enough to generate efficient ionization and charging, but that is still large enough to generate efficient luminescence at room temperature. Here we estimate that the optimum E_q should be around 0.2 ~ 0.3 eV and in the VRBE diagram $E_{5d1\text{-}CB}$ should be around 0.6 eV. This result means that the x=3, 3.5 and 4 samples have optimum E_q and the x=2.5 has acceptable E_q for efficient blue light charging.

There are different charging processes upon excitation to the higher 5*d* levels ($5d_2$, $5d_3$…) of Ce^{3+} because they are located within the CB or near the CB bottom. In the case of $5d_2$ excitation, we may distinguish two charging processes; process I is by means of thermal or autoionization from the $5d_2$ level to the CB, and in process II there is first a rapid relaxation to the $5d_1$ level followed by a thermally stimulated process to the CB as shown in Fig. 13. The probability of each process will depend on the relative energy location of the $5d_1$, $5d_2$ and the CB. For example, the TLE spectra in Fig. 10b for YAG:Ce-Cr (x=0) does not show the $5d_1$ TLE band. This is because of the large energy gap between the $5d_1$ level and the CB as can be seen in the VRBE diagram of Fig. 13. In this case, process II is not possible, and the $5d_2$ TLE band in Fig. 10 must be attributed to process I. At and above x=2.5, the charging process from the $5d_1$ level to the traps via the CB becomes possible as shown in Fig. 11. In this case also process II becomes possible.

Figure 6 shows that the TL peak temperature can be controlled between 150 K ~400 K. by varying the Ga concentration. This is because the VRBE E_{Cr}^{2+} of the trapped electron in the $3d^4$ ground state of Cr^{2+} does not change with Ga content, see column 7 of Table 4, while the VRBE E_C at the CB bottom lowers from -1.70 eV to -2.36 eV, see column 4 of Table 4. The reason why YAGG:Ce-Cr (x=1) has the highest TL peak temperature in column 2 with corresponding largest trap depth in column 3 of Table 2 is revealed in Fig. 13 which shows that the VRBE E_C at the CB bottom is highest for x=1, see also column 4 of Table 4. The broad range of detrapping temperatures and corresponding trap depths as demonstrated within the YAGG series of

compounds is useful for the design of phosphors with specific properties. For application as storage phosphors and persistent phosphors at high temperature, YAGG:Ce-Cr with x = 0 to 1 provides the best composition because the electron traps are deep enough to be stable at room temperature. For application as persistent phosphors applied at room temperature and charged by blue light, YAGG:Ce-Cr with x=2.5~3.5 is the best composition because the electron trap depth matches the energy optimum for the thermally activated process at room temperature and optimum *E*q for blue light charging.

Conclusions

In Cr and Ce doped $Y_3Al_{5-x}Ga_xO_{12}$, Ce on a dodecahedral site acts as the recombination center and Cr^{3+} on an octahedral site as the trapping center. The VRBE diagram including the binding energies in Ce^{3+}, Cr^{2+}, VB and CB in the $Y_3Al_{5-x}Ga_xO_{12}$ (x=0, 1, 2, 2.5, 3, 3.5, 4, 5) has been constructed. The Ce^{3+} luminescence quenching process in YAGG:Ce has been attributed to a thermal ionization process, and a correlation between the activation energy of the quenching process and the energy gap between the $5d_1$ level and the bottom of the CB was established. The activation energy for quenching directly affects the charging efficiency, and the optimum value for efficient charging is estimated around 0.2 eV ~0.3 eV. This translates to about 0.6 eV as the optimum energy gap between the $5d_1$ level and the bottom of the CB in the VRBE diagram. This activation energy and energy gap might well be a universal value for an efficient charging process and high persistent luminescence performance in all types of persistent phosphors. On the one hand the energy gap is small enough to generate charging by thermal activation at room temperature and on the other hand the energy gap is large enough to not fully quench the recombination luminescence at room temperature. By varying the Ga content the TL glow peak temperature can be controlled from 150 K to 400 K for glow curves measured at 10 K/min. The corresponding trap depths vary from 0.41 eV to 1.2 eV. It was found that the VRBE of the trapped electron in Cr^{2+} remains almost the same but the VRBE at the CB bottom decreases with increasing Ga content. Therefore, both the charging and the detrapping processes can be controlled by band gap and defect level engineering. A trap depth distribution with a width that that changes with Ga content was observed in $Y_3Al_{5-x}Ga_xO_{12}$:Ce-Cr. The width is minimum for x=0, x=3, and x=5 which was explained by the statistics in the distribution of the Ga ions on the sites around the Cr defect. From simulating the distribution we conclude that Ga first start to occupy the tetrahedral sites and above x=3 also the octahedral sites are being occupied.

Acknowledgements

This work was supported by JSPS KAKENHI Grant Numbers 25810136 and Project of Strategic Young Researcher Overseas Visits Program for Accelerating Brain Circulation (International Network-hub for Future Earth: Research for Global Sustainability).

Notes and references

[a] Graduate School of Human and Environmental Studies, Kyoto University, Kyoto 606-8501, Japan. Email:ueda.jumpei.5r@kyoto.ac.jp

[b] Graduate School of Global Environmental Studies, Kyoto University, Kyoto 606-8501, Japan

[c] Luminescence Materials Research Group, section FAME-RST, Faculty of Applied Sciences, Delft University of Technology, 2629 JB Delft, Netherlands

†Electronic Supplementary Information (ESI) available: Analytical details about heating rate method and pre-heating method; simulation results of TL glow curves; TL glow curves of YAG:Ce-Cr by heating rate method and pre-heating method. See DOI: 10.1039/b000000x/

1 J. Ueda, S. Tanabe and T. Nakanishi, *J. Appl. Phys.*, 2011, **110**, 053102.
2 W. M. Yen, M. Raukas, S. A. Basun, W. van Schaik and U. Happek, *J. Lumin.*, 1996, **69**, 287-294.
3 E. Van der Kolk, S. A. Basun, G. F. Imbusch and W. M. Yen, *Appl. Phys. Lett.*, 2003, **83**, 1740-1742.
4 E. van der Kolk, P. Dorenbos, J. T. M. de Haas and C. W. E. van Eijk, *Phys. Rev. B*, 2005, **71**, 045121.
5 J. Ueda, K. Aishima and S. Tanabe, *Opt. Mater.*, 2013, **35**, 1952-1957.
6 P. Dorenbos, *J. Electrochem. Soc.*, 2005, **152**, 107-110.
7 T. Aitasalo, J. Hölsä, H. Jungner, M. Lastusaari and J. Niittykoski, *J. Phys. Chem. B*, 2006, **110**, 4589-4598.
8 J. Ueda, T. Nakanishi, Y. Katayama and S. Tanabe, *Phys. Stat. Sol. c*, 2012, **9**, 2322-2325.
9 F. Clabau, X. Rocquefelte, S. Jobic, P. Deniard, M. H. Whangbo, A. Garcia and T. Le Mercier, *Chem. Mater.*, 2005, **17**, 3904-3912.
10 Y. Murayama, N. Takeuchi, Y. Aoki and T. Matsuzawa, US Patents, 5.242.006, 1995.
11 T. Matsuzawa, Y. Aoki, N. Takeuchi and Y. Murayama, *J. Electrochem. Soc.*, 1996, **143**, 2670-2673.
12 Y. Aoki, Y. Hirata, S. Hidehiko, O. Takaya and T. Nobuyoshi, Japanese Patent, 208948, 1997.
13 Y. Lin, Z. Tang and Z. Zhang, *Mater. Lett.*, 2001, **51**, 14-18.
14 Y. Lin, Z. Tang, Z. Zhang and C. W. Nan, *Appl. Phys. Lett.*, 2002, **81**, 996-998.
15 Y. Lin, Z. Tang, Z. Zhang, X. Wang and J. Zhang, *J. Mater. Sci. Lett.*, 2001, **20**, 1505-1506.
16 H. Takasaki, S. Tanabe and T. Hanada, *J. Ceram. Soc. Jpn.*, 1996, **104**, 322-326.
17 A. J. J. Bos, R. M. van Duijvenvoorde, E. van der Kolk, W. Drozdowski and P. Dorenbos, *J. Lumin.*, 2011, **131**, 1465-1471.
18 P. Dorenbos, *Phys. Rev. B*, 2013, **87**, 035118.
19 P. Dorenbos and A. J. J. Bos, *Rad. Meas.*, 2008, **43**, 139-145.
20 T. Maldiney, A. l. Lecointre, B. Viana, A. l. Bessière, M. Bessodes, D. Gourier, C. Richard and D. Scherman, *J. Am. Chem. Soc.*, 2011, **133**, 11810-11815.
21 Y. Zhuang, J. Ueda and S. Tanabe, *J. Mater. Chem. C*, 2013, **1**, 7849-7855.
22 J. Ueda, K. Kuroishi and S. Tanabe, *Appl. Phys. Express*, 2014, **7**, 062201.
23 Y. Zorenko, V. Gorbenko, I. Konstankevych, A. Voloshinovskii, G. Stryganyuk, V. Mikhailin, V. Kolobanov and D. Spassky, *J. Lumin.*, 2005, **114**, 85-94.
24 Y. Zorenko, T. Voznyak, V. Gorbenko, E. Zych, S. Nizankovski, A. Dan'ko and V. Puzikov, *J. Lumin.*, 2011, **131**, 17-21.
25 Y. Zorenko, V. Gorbenko, E. Mihokova, M. Nikl, K. Nejezchleb, A. Vedda, V. Kolobanov and D. Spassky, *Rad. Meas.*, 2007, **42**, 521-527.
26 J. Ueda, K. Kuroishi and S. Tanabe, *Appl. Phys. Lett.*, 2014, **104**, 033519.
27 M. S. Akselrod, N. Agersnap Larsen, V. Whitley and S. W. S. McKeever, *J. Appl. Phys.*, 1998, **84**, 3364-3373.
28 J. T. Randall and M. H. F. Wilkins, *Proceedings of the Royal Society of London. Series A. Mathematical and Physical Sciences*, 1945, **184**, 365-389.
29 J. T. Randall and M. H. F. Wilkins, *Proceedings of the Royal Society of London. Series A. Mathematical and Physical Sciences*, 1945, **184**, 390-407.
30 A. J. J. Bos, *Rad. Meas.*, 2006, **41**, S45-S56.
31 K. Van den Eeckhout, A. J. J. Bos, D. Poelman and P. F. Smet, *Phys. Rev. B*, 2013, **87**, 045126.
32 M. Marezio, J. P. Remeika and P. D. Dernier, *Acta Crystallographica Section B*, 1968, **24**, 1670-1674.

33 A. Nakatsuka, A. Yoshiasa and T. Yamanaka, *Acta Crystallographica Section B*, 1999, **55**, 266-272.
34 P. Dorenbos, *J. Lumin.*, 2013, **135**, 93-104.
35 P. Dorenbos, *J. Lumin.*, 2013, **134**, 310-318.
36 V. Babin, K. Blazek, A. Krasnikov, K. Nejezchleb, M. Nikl, T. Savikhina and S. Zazubovich, *Phys. Stat. Sol. c*, 2005, **2**, 97-100.
37 Y. Zorenko, T. Zorenko, V. Vistovskyy, M. Grinberg and T. Łukasiewicz, *Opt. Mater.*, 2009, **31**, 1835-1838.
38 A. Mayolet, W. Zhang, E. Simoni, J. C. Krupa and P. Martin, *Opt. Mater.*, 1995, **4**, 757-769.
39 P. Y. Jia, J. Lin, X. M. Han and M. Yu, *Thin Solid Films*, 2005, **483**, 122-129.
40 J. Ueda, K. Kuroishi and S. Tanabe, *Proc. SPIE 8987, Oxide-based Materials and Devices V*, 2014, **8987**(1-7).
41 L. Wang, X. Zhang, Z. Hao, Y. Luo, X.-j. Wang and J. Zhang, *Opt. Express*, 2010, **18**, 25177-25182.
42 M. Yamaga, Y. Oda, H. Uno, K. Hasegawa, H. Ito and S. Mizuno, *J. Appl. Phys.*, 2012, **112**, 063508(1-12).
43 E. G. Rogers and P. Dorenbos, *ECS J. Solid. State Sci. Technol.*, 2014, **3**, R173-R184.
44 E. G. Rogers and P. Dorenbos, *J. Lumin.*, 2014, **153**, 40-45.
45 E. G. Rogers and P. Dorenbos, *J. Lumin.*, 2014, **155**, 135-140.
46 P. Dorenbos and E. G. Rogers, *ECS J. Solid. State Sci. Technol.*, 2014, **3**, R150-R158.
47 H. H. Tippins, *Phys. Rev. B*, 1970, **1**, 126-135.
48 E. Loh, *J. Phys. Chem.*, 1966, **44**, 1940-1945.
49 V. A. Pustovarov, V. S. Kortov, S. V. Zvonarev and A. I. Medvedev, *J. Lumin.*, 2012, **132**, 2868-2873.

Graphical abstract

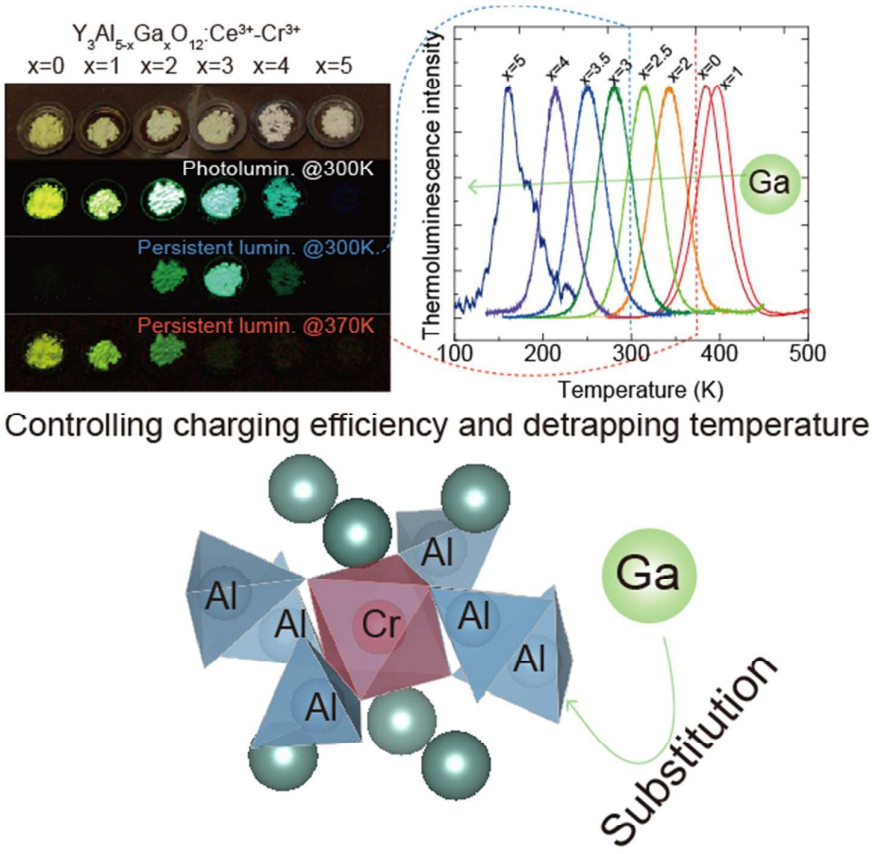

●Charging efficiency by blue light and trap depth were controlled by conduction band engineering in $Y_3Al_{5-x}Ga_xO_{12}$:Ce^{3+}-Cr^{3+}.